




Cite this: DOI: 10.1039/d3tc00152k

Strengthening the non-pre-irradiated near-infrared mechanoluminescence of CaZnOS:Nd³⁺ by Mn²⁺ coactivation for biomechanical imaging†

Jianxiong Lei, Wei Li, Yiqian Tang, Yiyu Cai, Shanshan Wang,* Kunpeng Dou and Jun-Cheng Zhang *

The development of lanthanide-activated CaZnOS mechanoluminescent (ML) phosphors that can produce non-pre-irradiated mechanoluminescence (ML) in the near-infrared (NIR) region opens a new avenue for *in vivo* and *in situ* biomechanical imaging. However, the progress in obtaining NIR ML images with a high signal-to-background ratio (SBR) has been constrained by the difficulties in achieving intense NIR ML. In this paper, we report a Mn²⁺-coactivation induced dual sensitization strategy that combines host sensitization with dopant sensitization to enhance the NIR ML of CaZnOS:Nd³⁺. Systematic characterization of the CaZnOS:Nd³⁺,Mn²⁺ series reveals that the enhanced NIR ML arises from the energy transfer from the host to Mn²⁺ to Nd³⁺, which involves the Mn²⁺-doping strengthened host excitation and the resonant energy transfer from Mn²⁺ to Nd³⁺. We demonstrate that the developed CaZnOS:Nd³⁺,Mn²⁺ phosphor greatly enhances the transient intensity of the NIR ML response and the SBR value of NIR ML images through a series of NIR ML penetration experiments on chicken breast and human cheek. In particular, the transient NIR ML response to dental occlusion is improved by 368%, while the SBR value of NIR ML penetrating the human cheek is improved from 1.25 to 2.1. Our results are expected to provide new insights into the development and optimization of non-pre-irradiated NIR ML phosphors, and further to advance the applications of NIR ML phosphors with an intense emission for high SBR biomechanical imaging.

Received 13th January 2023,
Accepted 1st February 2023

DOI: 10.1039/d3tc00152k

rsc.li/materials-c

Introduction

Mechanoluminescent (ML) materials are a class of energy conversion phosphors that can convert mechanical energy into light emission.^{1,2} Over the past two decades, ML materials with intense emission and quantitative mechanical-to-optical conversion have been rapidly developed.^{1,6} The existing ML materials can emit different colors in the visible region, with the representative ones including ZnS:Co²⁺,Ag⁺ (blue),⁷ CaZr(PO₄)₂:Eu²⁺ (cyan),⁸ BaSi₂O₂:N₂:Eu²⁺ (blue-green),⁹ SrAl₂O₄:Eu²⁺ (green),⁶ ZnS:Mn²⁺ (yellow),⁵ ZnS:Cu (orange),¹⁰ and NaNbO₃:Pr³⁺ (red).¹¹ These materials have been fabricated into various stress sensors and stress-driven light sources, showing promising applications in many fields, such as stress distribution visualization,^{12–14} structural health diagnosis,^{15–17} lighting,^{18,19} display,^{20–22} anti-counterfeiting,^{23–25} sono-optogenetics,^{7,26,27} and device operation.²⁸ Despite

remarkable achievements in visible ML materials, ML materials in the near-infrared (NIR) region (~700–2500 nm) are still lacking, even though the growing demand for the emerging applications in biomechanical imaging (that is, *in vitro* visualization of the mechanical property distributions of tissues *in vivo* and *in situ*).^{29–31} A few NIR ML materials have been reported in recent years, including Sr₃Sn₂O₇:Nd³⁺, SrAl₂O₄:Eu²⁺,Cr³⁺,Nd³⁺, LiNbO₃:Nd³⁺ and SrGa₁₂O₁₉:Cr³⁺.^{32–35} However, due to the trap-controlled ML features,^{1–4} these materials face the obstacle of requiring pre-irradiation charging prior to use. Once placed inside an organism, such trap-controlled ML materials cannot be easily recharged by external photoexcitation (*e.g.*, ultraviolet light).^{7,28} Therefore, research and development of NIR ML materials that do not require pre-irradiation charging is urgent for biomechanical imaging of deep tissues.

The family of CaZnOS-based phosphors is the only class of ML materials found to date that can emit NIR ML under non-pre-irradiated conditions.^{1–4} In 2013, the first ML material of this family, CaZnOS:Mn²⁺, was reported.³⁶ Since then, CaZnOS-based phosphors have attracted increasing attention due to two unique ML characteristics.^{37–43} One is that the ML generation of CaZnOS-based phosphors can be achieved without requiring

College of Physics and Optoelectronic Engineering, Ocean University of China, Qingdao 266100, China. E-mail: wangshanshan@ouc.edu.cn, zhangjuncheng@ouc.edu.cn

† Electronic supplementary information (ESI) available. See DOI: <https://doi.org/10.1039/d3tc00152k>

pre-irradiation charging,^{44–47} which is convenient for *in vivo* use. Another is that the CaZnOS host can be activated by a variety of luminescent ions, including transition metal ions (Mn^{2+} , Cu^{2+} , and Bi^{3+}) and lanthanide ions ($\text{Ln}^{3+} = \text{Pr}^{3+}$, Nd^{3+} , Sm^{3+} , Eu^{3+} , Tb^{3+} , Dy^{3+} , Ho^{3+} , Er^{3+} , Tm^{3+} , and Yb^{3+}), producing tunable ML across the visible and NIR regions.^{47–49} Among them, Nd^{3+} , Ho^{3+} , and Er^{3+} are the NIR activators, rendering CaZnOS particularly useful for biomechanical imaging.^{50,51} A typical application of non-pre-irradiated NIR ML is the recent report that CaZnOS: Nd^{3+} was used to monitor the severity of artificial cardiovascular occlusion and hypertension in rats by *in vitro* imaging.⁵² However, due to the intrinsic characteristics of Ln^{3+} ions, a small absorption cross-sectional area and a parity-forbidden 4f transition,^{53,54} the NIR ML intensity of Ln^{3+} -activated CaZnOS is currently limited at a low level, far from enabling biomechanical imaging with a high signal-to-background ratio (SBR).^{32,52} To improve the ML intensity of CaZnOS-based phosphors, flux-assisted solid-state reactions were developed to increase the crystallinity of the materials and the doping concentration of the activators.^{47,55} Despite being effective, the materials synthesized by this approach are still insufficient to achieve high SBR for biomechanical imaging. Therefore, strengthening the NIR ML intensity of non-pre-irradiated ML materials (*e.g.*, CaZnOS: Nd^{3+}) and further achieving a high SBR for biomechanical imaging remain a great challenge.

Herein, we present a Mn^{2+} -coactivation strategy that combines host sensitization with dopant sensitization to enhance the NIR ML of CaZnOS: Nd^{3+} (Fig. 1). The use of a Mn^{2+} co-activator is inspired by advances in bandgap engineering and photoluminescence (PL).^{37,56} First, Mn^{2+} doping can reduce the optical bandgap of CaZnOS,³⁷ which is expected to improve the marginal energy transfer from the host to the doped activators (Fig. 1(b)). Second, there is a spectral overlap between the PL emission spectrum of CaZnOS: Mn^{2+} (including the ${}^4\text{T}_1({}^4\text{G})\text{--}{}^6\text{A}_1({}^6\text{S})$ transition of Mn^{2+} and a weak host emission at ~ 520 nm) and the PL excitation spectrum of CaZnOS: Nd^{3+} (including the ${}^4\text{I}_{9/2}\text{--}{}^4\text{G}_{9/2}$, ${}^4\text{I}_{9/2}\text{--}{}^4\text{G}_{7/2}$, ${}^4\text{I}_{9/2}\text{--}{}^2\text{G}_{7/2}$, ${}^4\text{I}_{9/2}\text{--}{}^4\text{G}_{5/2}$, ${}^4\text{I}_{9/2}\text{--}{}^4\text{F}_{9/2}$ and ${}^4\text{I}_{9/2}\text{--}{}^4\text{F}_{7/2}$ transitions of Nd^{3+}) (Fig. 1(a)), which provides a precondition for the energy transfer from Mn^{2+} to Nd^{3+} . It should be noted that to the best of our knowledge, the sensitization strategy has never been evaluated in non-pre-irradiated ML materials, although it is commonly used for PL materials. We demonstrate that the superposition of the dual sensitization effects greatly enhances the NIR ML (900–1200 nm in NIR-I and NIR-II) of CaZnOS: Nd^{3+} , and further investigate the underlying mechanism of increase. We also demonstrate that the use of the developed CaZnOS: Nd^{3+} , Mn^{2+} phosphors can greatly improve the transient intensity of the NIR ML responses and enhance the SBR values of NIR ML images in biomechanical imaging.

Results and discussion

As a proof-of-concept experiment, we prepared a series of Nd^{3+} and/or Mn^{2+} doped CaZnOS phosphors using solid-state chemistry. The

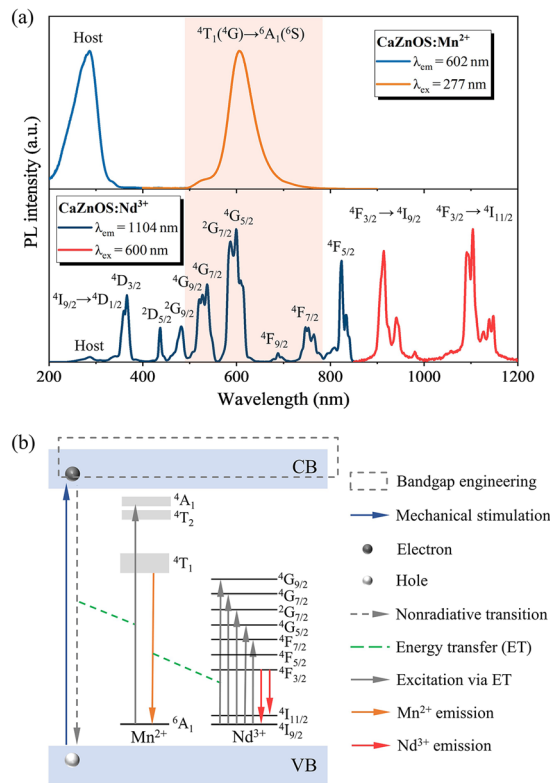


Fig. 1 Rational design of energy transfer to enhance the NIR ML of CaZnOS: Nd^{3+} . (a) PL excitation and emission spectra of CaZnOS: Mn^{2+} (top) and CaZnOS: Nd^{3+} (bottom). (b) Schematic illustration of the bandgap engineering and energy transfer pathway of ML in CaZnOS: Nd^{3+} , Mn^{2+} . VB: valence band; CB: conduction band.

general chemical formula of the target phosphors is $\text{Ca}_{1-x}\text{Nd}_x\text{Zn}_{1-y}\text{Mn}_y\text{OS}$ ($x = 0, 0.005; y = 0, 0.001, 0.003, 0.005, 0.007, \text{ and } 0.01$), abbreviated as CaZnOS:100x%Nd,100y%Mn. Unless otherwise stated, CaZnOS: Nd^{3+} refers to CaZnOS:0.5%Nd, and CaZnOS: Nd^{3+} , Mn^{2+} refers to CaZnOS:0.5%Nd,0.5%Mn. The X-ray diffraction patterns exhibit that the synthesized phosphors belong to the hexagonal CaZnOS phase (space group $P6_3mc$) (Fig. S1, ESI[†]).

The synthesized phosphors were next incorporated into composite disks and examined under mechanical stress. Both ML spectra and transient NIR ML responses were collected to systematically evaluate the ML properties. Notably, the main ML peaks of the CaZnOS: Nd^{3+} , Mn^{2+} series are located in the range of 500–1200 nm, and it is difficult to obtain ML spectra in this range with only one detector under the existing experimental conditions. Therefore, we used two CCD detectors in the ML tests. A silicon-based CCD detector was used to collect ML spectra in the range of 500–1000 nm containing visible ML emission of Mn^{2+} (${}^4\text{T}_1({}^4\text{G})\text{--}{}^6\text{A}_1({}^6\text{S})$) and NIR emission of Nd^{3+} (${}^4\text{F}_{3/2}\text{--}{}^4\text{I}_{9/2}$). An InGaAs-based CCD detector was used to collect ML spectra in the range of 900–1200 nm containing two NIR ML emissions of Nd^{3+} (${}^4\text{F}_{3/2}\text{--}{}^4\text{I}_{9/2}$ and ${}^4\text{F}_{3/2}\text{--}{}^4\text{I}_{11/2}$). In addition, we used a NIR single photon counting system (spectral response of 950–1700 nm and gate time of 20 ms) to capture the transient signals of the NIR ML in response to dynamic

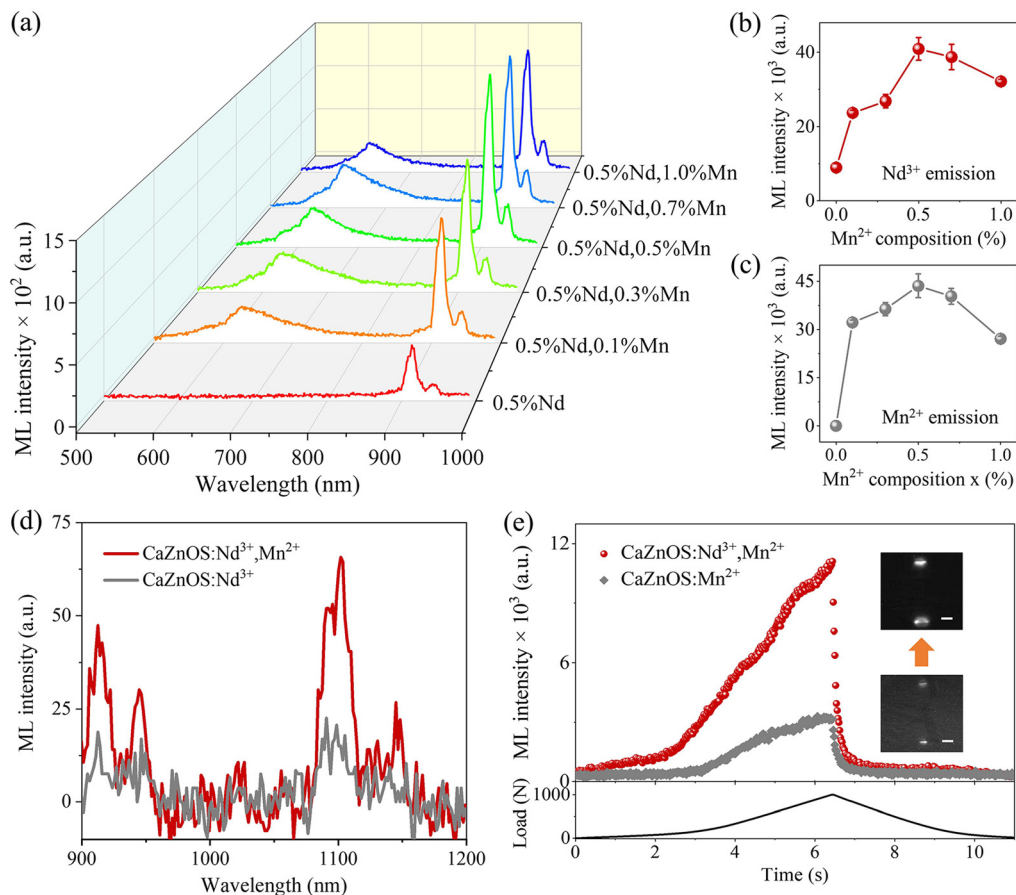


Fig. 2 Enhanced NIR ML of CaZnOS:Nd³⁺ by Mn²⁺ doping in the compressive test (load of 0–1000 N with a deformation rate of 5 mm min⁻¹). (a) ML spectra of CaZnOS:Nd³⁺,Mn²⁺ series collected in the range of 500–1000 nm. (b) and (c) Integrated ML intensity of Nd³⁺ (b) and Mn²⁺ (c) as a function of Mn²⁺ concentration in CaZnOS:Nd³⁺,Mn²⁺. (d) Compression-induced ML spectra of CaZnOS:0.5%Nd³⁺ and CaZnOS:0.5%Nd³⁺,0.5%Mn²⁺. (e) Transient NIR ML responses of CaZnOS:0.5%Nd³⁺ and CaZnOS:0.5%Nd³⁺,0.5%Mn²⁺ during the compression-release process. The inset shows the compression-induced NIR ML images of CaZnOS:0.5%Nd³⁺ (bottom) and CaZnOS:0.5%Nd³⁺,0.5%Mn²⁺ (top). Scale bars: 3 mm.

mechanical stimulation. To the best of our knowledge, there is no report on the transient ML responses of non-pre-irradiated NIR ML materials.^{47,50–52}

We first performed a compression-induced ML test. As expected, Mn²⁺ doping significantly increases the NIR ML intensity and the SBR values of the NIR ML images. The ML spectra collected in the range of 500–1000 nm show that Mn²⁺ doping not only activates the CaZnOS:Nd³⁺ phosphor to exhibit visible ML from Mn²⁺, but also enhances the NIR ML from Nd³⁺ (Fig. 2(a) and Fig. S2, ESI[†]). The NIR ML intensity of Nd³⁺ and the visible ML intensity of Mn²⁺ show similar trends to the Mn²⁺ concentration, and both reach the optimal ML intensity at 0.5%Mn²⁺ doping (Fig. 2(b and c)). The results suggest that the enhancement of the NIR ML of Nd³⁺ is closely related to doping of Mn²⁺. The ML spectra of Nd³⁺ collected in the range of 900–1200 nm exhibit that Mn²⁺ doping effectively enhances the two characteristic emissions of Nd³⁺ in the NIR-I region (⁴F_{3/2}–⁴I_{9/2}, 850–1000 nm) and the NIR-II region (⁴F_{3/2}–⁴I_{11/2}, 1000–1200 nm) (Fig. 2(d)). The transient responses of the NIR ML were also successfully collected during the dynamic compression–release process (Fig. 2(e)). The result shows that the

transient intensity of the NIR ML of CaZnOS:Nd³⁺,Mn²⁺ is linearly related to the applied compressive load, which can be used as a stress sensor. Moreover, the transient intensity of the NIR ML is greatly enhanced throughout the compression–release process, increasing by 256% at the peak loading of 1000 N (Fig. 2(e)). The NIR ML photographs were taken on a NIR camera. The photograph of CaZnOS:Nd³⁺,Mn²⁺ taken at the peak loading of 1000 N shows brighter NIR ML spots than that of CaZnOS:Nd³⁺ (insets of Fig. 2(e)). The SBR values of the NIR ML photographs are 2.38 for CaZnOS:Nd³⁺ and 13.42 for CaZnOS:Nd³⁺,Mn²⁺, showing an increase of 464% (Fig. S3, ESI[†]). These results indicate that Mn²⁺ coactivation effectively increases the SBR of the NIR ML of CaZnOS:Nd³⁺ in the compressive test.

We also performed a friction-induced ML test to further confirm the validity of Mn²⁺ doping in enhancing NIR ML. The ML spectra collected in the range of 500–1000 nm show that the NIR ML of Nd³⁺ is significantly improved by Mn²⁺ doping (Fig. 3(a) and Fig. S4, ESI[†]). The NIR ML intensity of Nd³⁺ and the visible ML intensity of Mn²⁺ show similar trends to the Mn²⁺ concentration, both reaching the maximum at 0.5%Mn²⁺

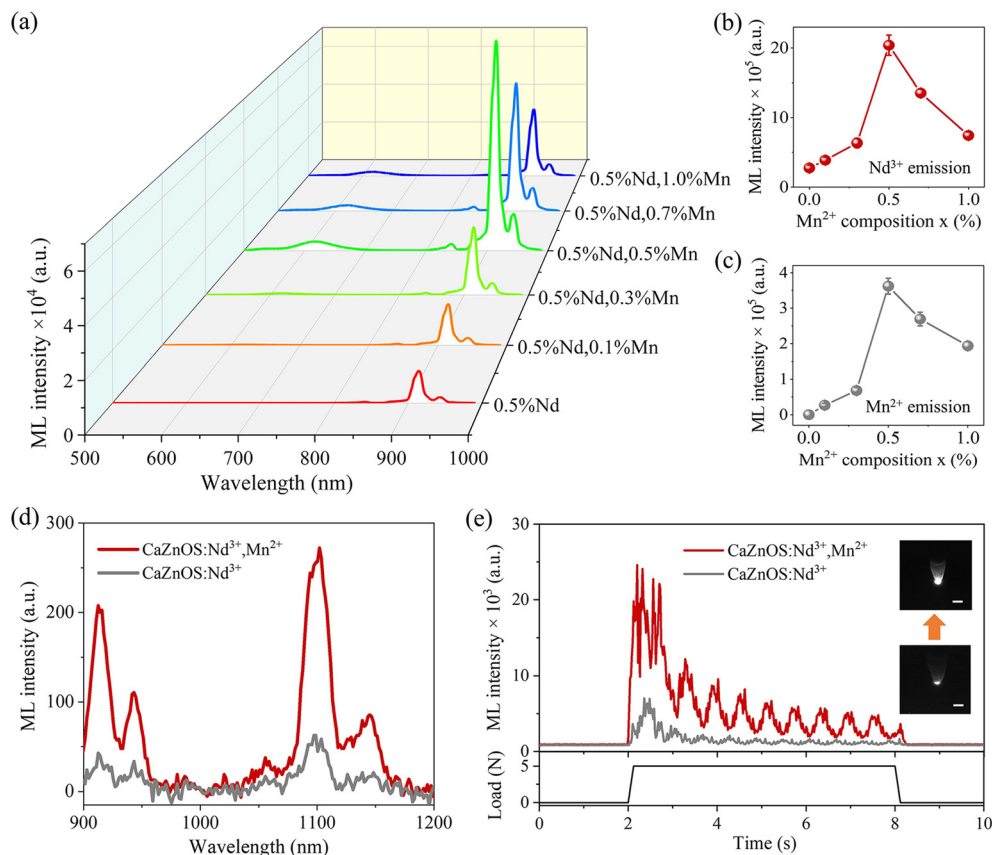


Fig. 3 Enhanced NIR ML of CaZnOS:Nd³⁺ by Mn²⁺ doping in the frictional test (frictional speed of 100 round min⁻¹ with a load of 5 N). (a) ML spectra of CaZnOS:Nd³⁺,Mn²⁺ series collected in the range of 500–1000 nm. (b) and (c) Integrated ML intensity of Nd³⁺ (b) and Mn²⁺ (c) as a function of Mn²⁺ concentration in CaZnOS:Nd³⁺,Mn²⁺. (d) Friction-induced ML spectra of CaZnOS:0.5%Nd³⁺ and CaZnOS:0.5%Nd³⁺,0.5%Mn²⁺. (e) Transient NIR ML responses of CaZnOS:0.5%Nd³⁺ and CaZnOS:0.5%Nd³⁺,0.5%Mn²⁺ during the frictional on-off process. The inset shows the friction-induced NIR ML images of CaZnOS:0.5%Nd³⁺ (bottom) and CaZnOS:0.5%Nd³⁺,0.5%Mn²⁺ (top). Scale bars: 3 mm.

doping (Fig. 3(b and c)). The ML spectra collected in the range of 900–1200 nm show that the characteristic emissions of Nd³⁺ are significantly enhanced by Mn²⁺ doping (Fig. 3(d)). The recorded transient ML signals indicate that the NIR ML of CaZnOS:Nd³⁺,Mn²⁺ has a fast linear response to the friction stimulation, and the transient intensity of the NIR ML of CaZnOS:Nd³⁺,Mn²⁺ is significantly higher than that of CaZnOS:Nd³⁺ during the whole friction process (Fig. 3(e) and Fig. S5, ESI[†]). These results are consistent with those obtained in the compression test, indicating that Mn²⁺ doping is an effective means to enhance the NIR ML of CaZnOS:Nd³⁺ under different mechanical stimuli. These results also suggest that the ML of CaZnOS-based phosphors induced by compression and friction may have a consistent mechano-optical conversion pathway.

To investigate the underlying mechanism of the NIR ML enhancement, we measured the reflectance spectra, PL spectra, and PL decay curves of the as-synthesized phosphor series (Fig. 4). The main findings include three aspects. First, the doping of Mn²⁺ narrows the optical bandgap of CaZnOS:Nd³⁺. The reflectance spectra show that the absorption edge of CaZnOS:Nd³⁺ is redshifted compared to CaZnOS:Nd³⁺,Mn²⁺ (Fig. 4(a)). The estimated results indicate the optical bandgap decreases from 3.56 eV for CaZnOS:0.5%Nd³⁺ to 3.43 eV for

CaZnOS:0.5%Nd³⁺,0.5%Mn²⁺ (Fig. S6, ESI[†]). The narrowing of the bandgap can reduce the energy level mismatch between the electron–hole recombination of the host and the characteristic excitation of the activator, thereby improving the marginal energy transfer from the host to the activator (*e.g.*, Mn²⁺). Second, the doping of Mn²⁺ significantly enhances the host excitation of Nd³⁺ emission. Comparison of the PL excitation spectra of CaZnOS:Nd³⁺,Mn²⁺ with different Mn²⁺ concentrations shows that the enhancement of NIR emission (850–1200 nm) of Nd³⁺ originates from the escalation of the host excitation (200–340 nm) caused by Mn²⁺ doping (Fig. S7, ESI[†]). The PL emission spectra show that the integrated intensity of the NIR emission of CaZnOS:0.5%Nd³⁺,0.5%Mn²⁺ is 15.85 times higher than that of CaZnOS:0.5%Nd³⁺ under the host excitation at 277 nm (Fig. 4(b)). Considering the small absorption cross-sectional area of Nd³⁺, we inferred that the excitation energy of the host should be mainly absorbed by Mn²⁺, and then Mn²⁺ transfers energy to Nd³⁺. Third, Mn²⁺ transfers energy to Nd³⁺ through a resonance mechanism. The PL decay curves show that Mn doping increases the average decay time of the ⁴F_{3/2}–⁴I_{9/2} transition of Nd³⁺ (Fig. 4(c) and Table S1, ESI[†]). The average decay time of Nd³⁺ emission is extended from 0.829 ms for CaZnOS:0.5%Nd³⁺ to 1.369 ms for CaZnOS:0.5%Nd³⁺,0.5%Mn²⁺. It

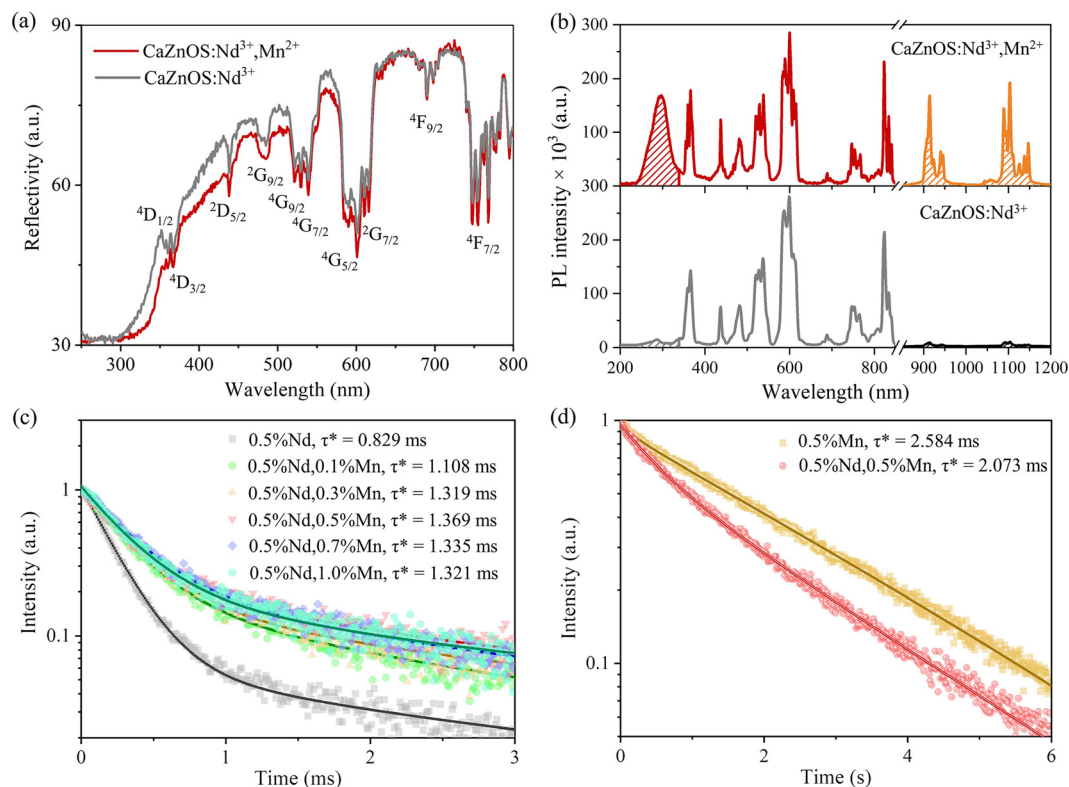


Fig. 4 Mechanistic investigation of energy transfer in CaZnOS:Nd³⁺,Mn²⁺. (a) Diffuse reflection spectra of CaZnOS:0.5%Nd³⁺,0.5%Mn²⁺ and CaZnOS:0.5%Nd³⁺. (b) PL excitation and emission spectra of CaZnOS:0.5%Nd³⁺,0.5%Mn²⁺ (top) and CaZnOS:0.5%Nd³⁺ (bottom) ($\lambda_{\text{ex}} = 277$ nm, $\lambda_{\text{em}} = 914$ nm). (c) PL decay curves and fitted average decay time of Nd³⁺ emission of CaZnOS:Nd³⁺,Mn²⁺ series with different Mn²⁺ concentrations ($\lambda_{\text{ex}} = 277$ nm, $\lambda_{\text{em}} = 914$ nm). (d) PL decay curves and the fitted average decay time of Mn²⁺ emission of CaZnOS:0.5%Mn²⁺ and CaZnOS:0.5%Nd³⁺,0.5%Mn²⁺ ($\lambda_{\text{ex}} = 277$ nm, $\lambda_{\text{em}} = 602$ nm).

suggests that Nd³⁺ absorbs additional energy, leading to an increase in the population of the ⁴F_{3/2} level of Nd³⁺. Furthermore, a control test monitoring the Mn²⁺ emission shows that the average decay time of the ⁴T₁(⁴G)–⁶A₁(⁶S) transition of Mn²⁺ is reduced from 2.584 ms for CaZnOS:0.5%Mn²⁺ to 2.074 ms for CaZnOS:0.5%Nd³⁺,0.5%Mn²⁺ (Fig. 4(d) and Table S1, ESI†). It suggests that Mn²⁺ transfers energy outward, decreasing the population of the ⁴T₁(⁴G) level of Mn²⁺. These lifetime-related results confirm that Mn²⁺ transfers energy to Nd³⁺ through a resonant mechanism.^{57,58} Taken these three findings together, we suggested that the doping of Mn²⁺ leads to the energy transfer of host → Mn²⁺ → Nd³⁺. Therefore, the enhancement of the non-pre-irradiated NIR ML of CaZnOS:Nd³⁺,Mn²⁺ could be explained as follows (Fig. 1(b)). Under the piezoelectric or triboelectric effect induced by mechanical stimulation, electrons are excited to the conduction band and simultaneously holes are generated in the valence band. The electron-hole pairs subsequently recombine and transfer energy to Mn²⁺. The narrowing of the bandgap caused by Mn²⁺ doping reduces the energy mismatch between the electron-hole recombination and the high-level excitation of Mn²⁺ (e.g., ⁶A₁–⁴T₂/⁴A₁), and thus the energy transfer from the host to Mn²⁺ is strengthened. Next, in addition to producing its own emission (i.e., ⁴T₁–⁶A₁), Mn²⁺ transfers energy to Nd³⁺ through a resonance process, leading to a significant enhancement of the NIR ML of Nd³⁺ (i.e., ⁴F_{3/2}–⁴I_{9/2} and ⁴F_{3/2}–⁴I_{11/2}).

To demonstrate the potential application of the developed CaZnOS:Nd³⁺,Mn²⁺ phosphor in biomechanical imaging, we performed imaging experiments with NIR ML penetrating fresh chicken breast and human cheek (Fig. 5). In the experiments of mechanical compression and friction, the ML composite pellets were covered with chicken breasts of different thicknesses (~2–20 mm), and NIR ML images and spectra were collected by penetrating the tissues (Fig. S8 and S9, ESI†). The NIR ML images show that the NIR ML of CaZnOS:Nd³⁺,Mn²⁺ has more powerful tissue-penetration ability compared to CaZnOS:Nd³⁺ (Fig. 5(a and d)). The compression- and friction-induced NIR ML of CaZnOS:Nd³⁺,Mn²⁺ is clearly imaged through 8 mm and 15 mm chicken breasts, respectively. In contrast, the penetrable thickness of the NIR ML of CaZnOS:Nd³⁺ is only 4 mm and 10 mm, respectively. In the case of covering with the same thickness of chicken tissues, the SBR values of the NIR ML images produced by CaZnOS:Nd³⁺,Mn²⁺ are consistently higher than those of CaZnOS:Nd³⁺ (Fig. S10 and S11, ESI†). The NIR ML spectra show that the enhanced ability of biomechanical imaging results from the significant enhancement of the NIR ML of CaZnOS:Nd³⁺,Mn²⁺ (Fig. 5(b,c and e,f)). In the *in vivo* experiments, we placed the food-grade insurance film-wrapped ML composites into a human mouth and gently bit the ML composites with teeth. The images, spectra and transient response of NIR ML penetrating the cheek were recorded during the biting process (Fig. S12, ESI†). The captured images show that

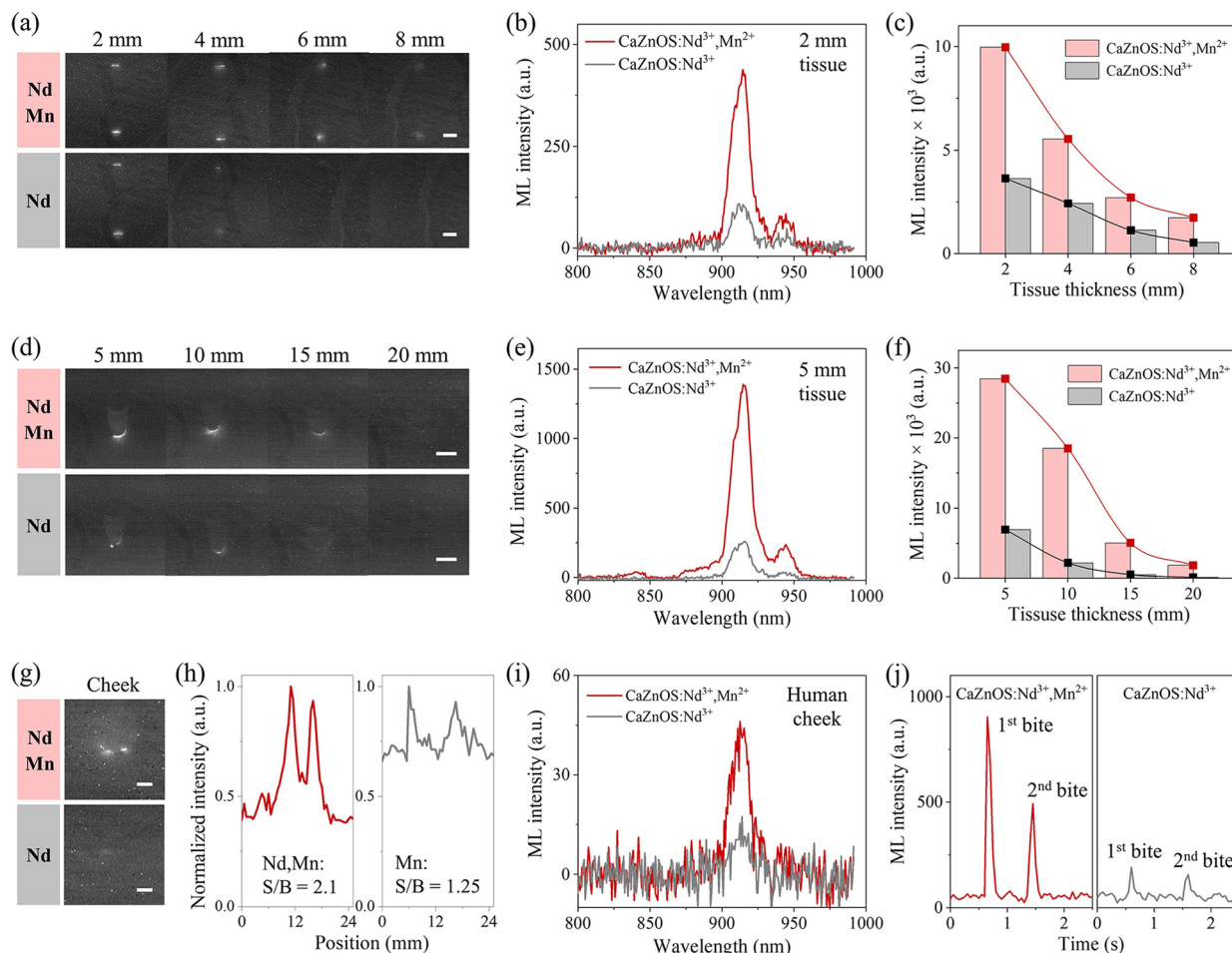


Fig. 5 Enhanced NIR ML of CaZnOS:Nd³⁺,Mn²⁺ for tissue-penetrating detection and biomechanical imaging. (a–c) Experiments on mechanical compression: images (a), spectra (b) and intensity (c) of the NIR ML of CaZnOS:0.5%Nd³⁺,0.5%Mn²⁺ and CaZnOS:0.5%Nd³⁺ covered with chicken breasts of different thicknesses (2, 4, 6 and 8 mm). (d–f) Experiments on mechanical friction: images (d), spectra (e) and intensity (f) of the NIR ML of CaZnOS:0.5%Nd³⁺,0.5%Mn²⁺ and CaZnOS:0.5%Nd³⁺ covered by chicken breasts with different thicknesses (5, 10, 15 and 20 mm). (g–j) Experiments on dental occlusion: images (g), SBR analysis (h), spectra (i) and transient response to double bites (j) of the NIR ML of CaZnOS:0.5%Nd³⁺,0.5%Mn²⁺ and CaZnOS:0.5%Nd³⁺ enclosed in the human oral cavity. Scale bars: 5 mm.

the NIR ML spots of CaZnOS:Nd³⁺,Mn²⁺ are clearly visible with an SBR value of 2.1, while the image of CaZnOS:Nd³⁺ is blurred with an SBR value of only 1.25 (Fig. 5(g and h)). The spectra and transient signals of the cheek-penetrating NIR ML in response to dental occlusion show that the intensity of the cheek-penetrating NIR ML of CaZnOS:Nd³⁺,Mn²⁺ is much higher than that of CaZnOS:Nd³⁺ (Fig. 5(i and j)). The integrated intensity of the NIR ML spectra of CaZnOS:Nd³⁺,Mn²⁺ is 396% higher than that of CaZnOS:Nd³⁺ (Fig. 5(i)), and the transient intensity of the NIR ML of CaZnOS:Nd³⁺,Mn²⁺ at the 1st bite peak is 368% higher than that of CaZnOS:Nd³⁺ (Fig. 5(j)). These results confirm that the SBR of biomechanical imaging is greatly improved by an effective increase of the NIR ML intensity of the phosphors.

Conclusions

In summary, our investigations on a series of Mn²⁺ co-activated CaZnOS:Nd³⁺ phosphors suggest a dual sensitization strategy

for enhancing the non-pre-irradiated NIR ML. We demonstrate that the co-activation of Mn²⁺ produces an energy transfer from the host to Mn²⁺ to Nd³⁺, which involves both host sensitization strengthened by bandgap engineering and dopant sensitization *via* resonance energy transfer from Mn²⁺ to Nd³⁺. The developed CaZnOS:Nd³⁺,Mn²⁺ phosphors enable the achievement of NIR ML images with high SBR in biomechanical imaging, including penetration of fresh chicken breast and human cheek. We expect to extend this prototype strategy in further studies to synthesize non-pre-irradiated NIR ML nanoparticles with intense emission and advance their applications in *in vivo* and *in situ* biomechanical imaging.

Experimental section

Synthesis

Polycrystalline materials with the chemical formula Ca_{1-x}Nd_xZn_{1-y}Mn_yOS ($x = 0, 0.005; y = 0, 0.001, 0.003, 0.005, 0.007,$

and 0.01), abbreviated as CaZnOS:100x%Nd,100y%Mn, were synthesized by solid-state chemistry among CaCO₃ (Aladdin, 99.99%), ZnS (Aladdin, 99.99%), Nd₂O₃ (Aladdin, 99.99%), MnCO₃ (Aladdin, 99.95%), and Li₂CO₃ (Aladdin, 99.99%). Li₂CO₃ is used as a flux at 6 wt% addition. The stoichiometric mixture was thoroughly ground, tableted, and then sintered in a horizontal tube furnace at 1100 °C for 3 h under an argon atmosphere. The prepared product was pulverized, ground, and screened through a 20-μm sieve to microparticles for later use.

Structural and optical characterization

X-ray diffraction measurements were carried out on an X-ray powder diffractometer (D8 Advance, Bruker AXS GmbH). Diffuse reflectance spectra were measured using an ultraviolet-visible spectrophotometer (TU-1901, Persee). The excitation spectra, emission spectra, and decay curves of photoluminescence were recorded on a fluorescence spectrometer (FLS-1000, Edinburgh Instruments Ltd).

Mechanoluminescent characterization

Composite cylinders of 25 mm in diameter and 15 mm in thickness were prepared by mixing the screened microparticles with a transparent epoxy resin (SpeciFix, Struers GmbH) at a 1:9 weight ratio. Mechanical compression and friction were applied using a universal testing machine (AGS-X, Shimadzu) and a friction testing machine (MS-T3001, Lanzhou Huahui), respectively. ML spectra were recorded with a high sensitivity spectrometer with a silicon-based CCD detector (QEPro, Ocean Optics) and a NIR spectrometer with an InGaAs-based CCD detector (NIRQuest, Ocean Optics). Transient NIR ML signals were collected with a NIR photon-counting system (H10330C-75, Hamamatsu Photonics K.K.). NIR ML photographs were taken with a NIR camera (C12741-03, Hamamatsu Photonics K.K.). It should be noted that all samples were not pre-irradiated with a light source prior to ML testing.

Conflicts of interest

The authors have no conflicts to disclose.

Acknowledgements

This work was supported by the National Natural Science Foundation of China (No. 11774189), the Fundamental Research Funds for the Central Universities, and the Shandong Provincial Natural Science Foundation (No. ZR2021MF123).

References

- J.-C. Zhang, X. Wang, G. Marriott and C.-N. Xu, *Prog. Mater. Sci.*, 2019, **103**, 678–742.
- Y. Tang, J. Lei, X. Zhang, S. Wang, X. Shi and J.-C. Zhang, *Chin. J. Lumin.*, 2021, **42**, 404–418.
- Y. Zhuang and R.-J. Xie, *Adv. Mater.*, 2021, **33**, 2005925.
- B. Chen, X. Zhang and F. Wang, *Acc. Mater. Res.*, 2021, **2**, 364–373.
- C.-N. Xu, T. Watanabe, M. Akiyama and X.-G. Zheng, *Appl. Phys. Lett.*, 1999, **74**, 1236–1238.
- C.-N. Xu, T. Watanabe, M. Akiyama and X.-G. Zheng, *Appl. Phys. Lett.*, 1999, **74**, 2414–2416.
- X. Wu, X. Zhu, P. Chong, J. Liu, L. N. Andre, K. S. Ong, K. B. Jr, A. I. Mahdi, J. Li, L. E. Fenno, H. Wang and G. Hong, *Proc. Natl. Acad. Sci. U.S.A.*, 2019, **116**, 26332–26342.
- J.-C. Zhang, C.-N. Xu and Y.-Z. Long, *Opt. Express*, 2013, **21**, 13699–13709.
- J. Botterman, K. V. D. Eeckhout, I. D. Baere, D. Poelman and F. Smet, *Acta Mater.*, 2012, **60**, 5494–5500.
- S. M. Jeong, S. Song, S.-K. Lee and N. Y. Ha, *Adv. Mater.*, 2013, **25**, 6194–6200.
- J.-C. Zhang, C. Pan, Y.-F. Zhu, L.-Z. Zhao, H.-W. He, X. Liu and J. Qiu, *Adv. Mater.*, 2018, **30**, 1804644.
- S. Timilsina, K. H. Lee, Y. N. Kwon and J. S. Kim, *J. Am. Ceram. Soc.*, 2015, **98**, 2197–2204.
- J. Jang, H. Kim, S. Ji, H. J. Kim, M. S. Kang, T. S. Kim, J.-E. Won., J.-H. Lee, J. Cheon, K. Kang, W. B. Im and J.-U. Park, *Nano Lett.*, 2019, **20**, 66–74.
- Y. Zhuang, X. Li, C. Chen, Z. Wu, H. Luo, L. Jin and R.-J. Xie, *Adv. Mater.*, 2022, **34**, 2202864.
- Y. Fujio, C.-N. Xu, Y. Terasawa, Y. Sakata, J. Yamabe, N. Ueno, N. Terasaki, A. Yoshida, S. Watanabe and Y. Murakami, *Int. J. Hydrogen Energy*, 2016, **41**, 1333–1340.
- L. Liu, C.-N. Xu, A. Yoshida, D. Tu, N. Ueno and S. Kainuma, *Adv. Mater. Technol.*, 2019, **4**, 1800336.
- M. A. S. Shohag, S. A. Tran, T. Ndebele, N. Adhikari and O. I. Okoli, *Mater. Des.*, 2018, **153**, 86–93.
- S. M. Jeong, S. Song, S.-K. Lee and B. Choi, *Appl. Phys. Lett.*, 2013, **102**, 051110.
- S. M. Jeong, S. Song, K.-I. Joo, J. Kim, S.-H. Hwang, J. Jeong and H. Kim, *Energy Environ. Sci.*, 2014, **7**, 3338–3346.
- X. Wang, H. Zhang, R. Yu, L. Dong, D. Peng, A. Zhang, Y. Zhang, H. Liu, C. Pan and Z. L. Wang, *Adv. Mater.*, 2015, **27**, 2324–2331.
- X. Qian, Z. Cai, M. Su, F. Li, W. Fang, Y. Li, X. Zhou, Q. Li, X. Feng, W. Li, X. He, X. Wang, C. Pan and Y. Song, *Adv. Mater.*, 2018, **30**, 1800291.
- X. Zhao, Z. Zhang, Q. Liao, X. Xun, F. Gao, L. Xu, Z. Kang and Y. Zhang, *Sci. Adv.*, 2020, **6**, eaba4294.
- J.-C. Zhang, N. Gao, L. Li, S. Wang, X. Shi, M. Sun, X. Yan, H.-W. He, X. Ning, B. Huang and J. Qiu, *Adv. Funct. Mater.*, 2021, **31**, 2100221.
- T. Jiang, Y.-F. Zhu, J.-C. Zhang, J. Zhu, M. Zhang and J. Qiu, *Adv. Funct. Mater.*, 2019, **29**, 1906068.
- Z. D. Ma, J. Zhou, J. Zhang, S. Zeng, H. Zhou, A. T. Smith, W. Wang, L. Sun and Z. Wang, *Mater. Horiz.*, 2019, **6**, 2003–2008.
- G. Hong, *Science*, 2020, **369**, 638.
- F. Yang, X. Wu, H. Cui, S. Jiang, Z. Ou, S. Cai and G. Huang, *J. Am. Chem. Soc.*, 2022, **144**, 18406–18418.
- B. Hou, L. Yi, C. Li, H. Zhao, R. Zhang, B. Zhou and X. Liu, *Nat. Electron.*, 2022, **5**, 682–693.

- 29 K. Hyodo, Y. Terasawa, C.-N. Xu, H. Sugaya, H. Mishima and S. Miyakawa, *J. Biomech.*, 2012, **45**, S263.
- 30 N. Terasaki, H. Yamada and C.-N. Xu, *Catal. Today*, 2013, **201**, 203–208.
- 31 P. E. Barbone and A. A. Oberai, A review of the mathematical and computational foundations of biomechanical imaging, ed. S. De, F. Guilak, M. R. K. Mofrad, *Computational Modeling in Biomechanics*, Springer, Dordrecht, 2010, pp. 375–408.
- 32 D. Tu, C.-N. Xu, S. Kamimura, Y. Horibe, H. Oshiro, L. Zhang, Y. Ishii, K. Hyodo, G. Marriott, N. Ueno and X.-G. Zheng, *Adv. Mater.*, 2020, **32**, 1908083.
- 33 Y. Fujio, C.-N. Xu and N. Terasaki, *ECS Trans.*, 2020, **98**, 61.
- 34 P. Xiong and M. Peng, *J. Mater. Chem. C.*, 2019, **7**, 6301–6307.
- 35 S. Liu, Y. Zheng, D. Peng, J. Zhao, Z. Song and Q. Liu, *Adv. Funct. Mater.*, 2023, **33**, 2209275.
- 36 J.-C. Zhang, C.-N. Xu, S. Kamimura, Y. Terasawa, H. Yamada and X. Wang, *Opt. Express.*, 2013, **21**, 12976–12986.
- 37 J.-C. Zhang, L.-Z. Zhao, Y.-Z. Long, H.-D. Zhang, B. Sun, W.-P. Han, X. Yan and X. Wang, *Chem. Mater.*, 2015, **27**, 7481–7489.
- 38 B. Huang, *Phys. Chem. Chem. Phys.*, 2016, **18**, 25946–25974.
- 39 C. Pan, J.-C. Zhang, M. Zhang, X. Yan, Y.-Z. Long and X. Wang, *Appl. Phys. Lett.*, 2017, **110**, 233904.
- 40 D. Tu, C.-N. Xu, Y. Fujio and A. Yoshida, *Light: Sci. Appl.*, 2015, **4**, e356–e356.
- 41 C. Chen, Y. Zhuang, D. Tu, X. Wang, C. Pan and R.-J. Xie, *Nano Energy*, 2020, **68**, 104329.
- 42 Y. Zhao, D. Peng, G. Bai, Y. Huang, S. Xu and J. Hao, *Adv. Funct. Mater.*, 2021, **31**, 2010265.
- 43 Y.-L. Yang, X.-C. Yang, J.-Y. Yuan, T. Li, Y.-T. Fan, L. Wang, Z. Deng, Q.-L. Li, D.-Y. Wan, J.-T. Zhao and Z.-J. Zhang, *Adv. Opt. Mater.*, 2021, **9**, 2100668.
- 44 L. Chen, M.-C. Wong, G. X. Bai, W. Jie and J. Hua, *Nano Energy*, 2015, **14**, 372–381.
- 45 Y. Zhang, X. Zhang, H. Wang, Y. Tian, H. Pan, L. Zhang, F. Wang and J. Chang, *Adv. Funct. Mater.*, 2021, **31**, 2006357.
- 46 S. Zhou, Y. Cheng, J. Xu, H. Lin, W. Liang and Y. Wang, *Laser Photonics Rev.*, 2022, **16**, 2100666.
- 47 Y. Du, Y. Jiang, T. Sun, J. Zhao, B. Huang, D. Peng and F. Wang, *Adv. Mater.*, 2019, **31**, 1807062.
- 48 J. Yuan, Y. Yang, X. Yang, Y. Fan, T. Li, M. Haung, F. Zhang, Q. Li, J. Zhao and Z. Zhang, *J. Mater. Chem. C.*, 2021, **9**, 7689–7696.
- 49 C. Wang, R. Ma, D. Peng, X. Liu, J. Li, B. Jin, A. Shan, Y. Fu, L. Dong, W. Gao, Z. Wang and C. Pan, *InfoMat*, 2021, **3**, 1272–1284.
- 50 L. Li, L. Wondraczek, L. Li, Y. Zhang, Y. Zhu, M. Peng and C. Mao, *ACS Appl. Mater. Interfaces*, 2018, **10**, 14509–14516.
- 51 L. Li, L. Wondraczek, M. Peng, Z. Ma and B. Zou, *Nano Energy*, 2020, **69**, 104413.
- 52 X. Liu, P. Xiong, L. Li, M. Yang, M. Yang and C. Mao, *Mater. Horiz.*, 2022, **9**, 1658–1669.
- 53 M. Zhang, W. Zheng, Y. Liu, P. Huang, Z. Guong, J. Wei, Y. Gao, S. Zhou, X. Li and X. Chen, *Angew. Chem., Int. Ed.*, 2019, **58**, 9556–9560.
- 54 W. Shao, G. Y. Chen, A. Kuzmin, H. L. Kutscher, A. Pliss, T. Y. Ohulchanskyy and P. N. Prasad, *J. Am. Chem. Soc.*, 2016, **138**, 16192–16195.
- 55 D. Tu, C.-N. Xu and Y. Fujio, *J. Adv. Dielectr.*, 2014, **4**, 1450017.
- 56 X. Zhang, Q. Zhu, B. Chen, S. Wang, A. L. Rogach and F. Wang, *Adv. Photonics Res.*, 2021, **2**, 2000089.
- 57 P. G. Wu and L. Brand, *Anal. Biochem.*, 1994, **218**, 1–13.
- 58 P. A. Tanner, L. Zhou, C. Duan and K.-L. Wong, *Chem. Soc. Rev.*, 2018, **47**, 5234–5265.